Journal of Catalysis 284 (2011) 23–33

Contents lists available at SciVerse ScienceDirect

Journal of Catalysis

journal homepage: www.elsevier.com/locate/jcat

Iron-substituted TNU-9, TNU-10, and IM-5 zeolites and their steam-activated analogs as catalysts for direct N_2O decomposition

Jun Kyu Lee [a], Young Jin Kim [a], Heung-Ju Lee [a], Su Hyun Kim [b], Sung June Cho [b], In-Sik Nam [a], Suk Bong Hong [a,*]

[a] School of Environmental Science and Engineering and Department of Chemical Engineering, POSTECH, Pohang 790-784, Republic of Korea
[b] Department of Applied Chemical Engineering, Chonnam National University, Gwangju 500-757, Republic of Korea

ARTICLE INFO

Article history:
Received 18 June 2011
Revised 24 August 2011
Accepted 25 August 2011
Available online 10 October 2011

Keywords:
Iron-substituted zeolites
Steaming
N_2O decomposition activity
Framework structure

ABSTRACT

Isomorphously substituted Fe-TNU-9, Fe-TNU-10, and Fe-IM-5 zeolites containing both Fe and Al in framework positions have been hydrothermally synthesized and tested as catalysts for direct N_2O decomposition, together with their steam-activated analogs. When compared with the catalytic results obtained from the corresponding forms of Fe-ZSM-5 with a similar Fe content, the specific activity per mole of iron is higher in the order Fe-TNU-10 < Fe-IM-5 < Fe-TNU-9 < Fe-ZSM-5. While all these catalysts have a promoting effect of NO on N_2O decomposition, they exhibit different extents of increase in activity by NO addition, suggesting differences in the type of their extra-framework iron species. From the overall characterization results of our study, we can conclude that the thermal stability of Fe in framework positions differs notably according to the structure type of zeolites, which may have an intrinsic effect upon the nature and distribution of extra-framework iron species, and thus upon their N_2O decomposition activity.

1. Introduction

N_2O is a powerful greenhouse gas whose global warming potential is 310 and 15 times higher than that of CO_2 and CH_4, respectively. Hence, it is not so surprising that this gas has long been included in the six-gas basket defined by the United Nations Framework Convention on Climate Change [1]. Considering its indirect contribution to the ozone layer depletion as the main precursor of stratospheric NO_x [2,3], the harmful effects of N_2O are even more manifest. Over the past several decades, therefore, many strategies to reduce N_2O emissions have been proposed and explored [4]. Because the temperature of waste streams from many chemical processes is usually below 450 °C, much attention has been devoted to the development of efficient catalyst systems that can remove N_2O at temperatures as low as possible. Among them, direct catalytic decomposition of N_2O and its selective catalytic reduction by hydrocarbons are being considered as the two most proper technologies to remove this harmful gas from industrial waste streams [5]. Since the external supply of hydrocarbons is expensive, however, the former technology is more cost-efficient.

Iron-containing zeolites are of great technological relevance because they are potentially useful catalysts for many chemical reactions of environmental and industrial interests—for instance, selective reduction of NO_x by ammonia and hydrocarbons, selective oxidation of benzene to phenol with N_2O, and oxidative dehydrogenation of propane to propene [6–15]. This is particularly the case for direct decomposition of N_2O into N_2 and O_2 [16–21]. One well-established means for preparing more catalytically active iron zeolites is the isomorphous replacement of Al by Fe in the zeolite framework during the crystallization process and the subsequent steaming of the resulting materials [22,23]. Indeed, this method has been repeatedly shown to generate a highly homogeneous distribution of oxidic iron species upon Fe extraction from the zeolite framework, giving steam-activated, iron-substituted zeolites notably high turnover frequencies in N_2O decomposition compared with those of iron-containing zeolites prepared by (aqueous or solid) ion exchange or sublimation followed by steaming [16,24].

The great success of ZSM-5 (framework type MFI) as a shape-selective catalyst in many petrochemical and refining processes is largely due to its unique three-dimensional (3D) 10-ring pore system. Thus, considerable effort has been directed toward the synthesis of new multidimensional medium-pore zeolite structures. Unlike the cases of small- and large-pore materials, however, a relatively smaller number of 10-ring zeolites have been discovered thus far. The new medium-pore zeolites recently reported include TNU-9 (TUN), TNU-10 (STI), and IM-5 (IMF), all of which have been synthesized in the presence of a flexible linear diquaternary alkylammonium cation composed of two *N*-methylpyrrolidinium

* Corresponding author. Fax: +82 54 2798299.
E-mail address: sbhong@postech.ac.kr (S.B. Hong).

0021-9517/$ - see front matter © 2011 Elsevier Inc. All rights reserved.
doi:10.1016/j.jcat.2011.08.012

groups connected by a tetra- or pentamethylene chain [25–29]. While the projection of TNU-9 down the *b*-axis, along which two slightly wider and narrower 10-ring channels are extended, is similar to that of ZSM-5, the channel connectivity in the third direction is more complex. TNU-10 is a high-silica version of (Si/Al = 7.1) of the natural zeolite stilbite (STI) with two intersecting 10-ring and 8-ring channels. Because all natural STI-type zeolites possess relatively low Si/Al ratios (<3.6) and thus poor thermal stability, on the other hand, little is known of their catalytic and adsorption properties. Although IM-5 has a 3D 10-ring channel system, its channel connectivity is very complex, in addition, imparting the character of a 2D pore system with restricted diffusion to this medium-pore zeolite. Therefore, it is not difficult to expect that the shape-selective properties of these three zeolites are substantially different from those observed for ZSM-5.

In this contribution we report the hydrothermal synthesis of Fe-TNU-9, Fe-TNU-10, and Fe-IM-5 zeolites containing both Fe and Al in framework positions and the catalytic properties of their proton and steam-activated forms for N_2O decomposition. The introduction of heteroatoms other than Al into the zeolite framework is of practical importance, because it can shift catalytically useless materials into catalysts quite active for particular types of chemical reactions. To our knowledge, however, no attempts have yet been made to isomorphously replace Al with heteroatoms in the framework of TNU-9, TNU-10, or IM-5. To examine the effects of zeolite structure on the nature and distribution of extra-framework iron species and hence on their N_2O decomposition activity, the physicochemical properties of all iron-containing zeolites prepared here have been characterized using various analytical methods including NH_3 temperature-programmed desorption, transmission electron microscopy, UV–vis spectroscopy, X-ray absorption fine structure spectroscopy, and electron spin resonance. The characterization results are compared with those obtained from an isomorphously substituted Fe-ZSM-5 with similar Fe content, as well as from Fe-TNU-9 and Fe-ZSM-5 prepared by the $FeCl_3$ sublimation method.

2. Experimental

2.1. Synthesis

1,4-Bis(*N*-methylpyrrolidinium)butane (1,4-MPB) and 1,5-bis (*N*-methylpyrrolidinium)pentane (1,5-MPP) in their bromide forms were prepared, purified, and characterized as described in our previous papers [26,29]. These two diquaternary ammonium salts were stored in a desiccator before use as organic structure-directing agents (SDAs).

The synthesis of iron-substituted zeolites using 1,4-MPB or 1,5-MPP was carried out using gels prepared by combining NaOH (50% aqueous solution, Aldrich); $Al(NO_3)_3{\cdot}9H_2O$ (98%, Junsei) and/or $Fe(NO_3)_3{\cdot}9H_2O$ (98%, Aldrich); fumed silica (Aerosil 200, Degussa); and deionized water. The final gel composition was $4.5R{\cdot}xNa_2O{\cdot}yFe_2O_3{\cdot}(0.5-y)Al_2O_3{\cdot}30SiO_2{\cdot}1200H_2O$, where *R* is 1,4-MPB or 1,5-MPP, *x* is 11.0 or 15.0, and $0 \leqslant y \leqslant 0.5$. After being stirred at room temperature for 1 day, the final synthesis mixture was transferred to Teflon-lined 45-cm^3 autoclaves and heated at 160 °C under rotation (100 rpm) for 7–21 days. The solid products were recovered by filtration, washed repeatedly with distilled water, and dried overnight at room temperature. As-made zeolites were calcined in air at 550 °C for 8 h to remove the occluded organic SDA. The calcined samples were then refluxed twice in 1.0 M NH_4NO_3 solutions for 6 h, followed by calcination at 550 °C for 4 h to obtain their proton forms. For comparison, an isomorphously substituted Fe-ZSM-5 with both Fe (1.4 wt%) and Al in framework positions was synthesized according to the procedures given elsewhere [30]. Also, Fe-TNU-9 and Fe-ZSM-5 were prepared by $FeCl_3$ sublimation. The parent zeolites were H-TNU-9 with Si/Al = 20 and H-ZSM-5 with Si/Al = 27, prepared following the procedures developed by our group [26] and obtained from Tosoh, respectively. Further details of the sublimation procedure can be found in our previous work [19].

Steam activation was carried out in accordance with a procedure similar to that reported in the literature [16,30,31]. Iron-containing zeolites were placed inside a U-shaped quartz reactor and heated under atmospheric pressure and flowing He (55 $cm^3\ min^{-1}$) at a rate of 2 °C min^{-1} to a final temperature of 600 °C. After the He flow was replaced with 40% steam in He (55 $cm^3\ min^{-1}$), the reactor was kept at this temperature for 5 h. Finally, the steamed solids were allowed to return to room temperature under flowing He at a rate of 2 °C min^{-1}. The as-made, proton, and steam-activated forms of zeolites prepared here were designated by hyphenating the prefixes *am*, H, and *s* to their general names. To distinguish between the iron zeolites prepared by hydrothermal synthesis and those by sublimation, in addition, the suffix HS or S was attached in parentheses to their names. For example, *s*-Fe-TNU-9(HS) indicates the steam-activated form of Fe-TNU-9 zeolite prepared by hydrothermal synthesis.

2.2. Catalytic experiments

N_2O decomposition activity measurements were performed under atmospheric pressure in a conventional fixed flow reactor. A sample of 0.5 g of zeolite catalyst were sieved into a mesh size of 20/30 to minimize the mass transfer limitations, activated under flowing air (560 $cm^3\ min^{-1}$) at 550 °C for 2 h, and cooled to the initial reaction temperature (350 °C). Then a gas mixture consisting of 1000 ppm N_2O and 4% O_2 in N_2 balance, with or without 10% H_2O present, was fed into the reactor system. If necessary, 200 ppm NO was also introduced. The total flow rate at the reactor inlet was kept constant at 560 $cm^3\ min^{-1}$, corresponding to a GHSV of 42,000 h^{-1}, and the N_2O decomposition activity was examined in the temperature range 350–550 °C. The inlet and outlet gas concentrations were analyzed on line using a Nicolet 5700 FT-IR spectrometer equipped with a 2-m gas cell. The N_2O conversion is defined as follows:

$$N_2O\ \text{conversion}\ (\%) = ([N_2O]_{\text{inlet}} - [N_2O]_{\text{outlet}})/[N_2O]_{\text{inlet}} \times 100\ (\%).$$

2.3. Characterization

Product phase identification was carried out by powder X-ray diffraction (XRD) on a PANalytical X'Pert diffractometer (Cu Kα radiation) with an X'Celerator detector. Elemental analysis for Si, Al, and Fe was carried out by a Jarrell-Ash Polyscan 61E inductively coupled plasma spectrometer in combination with a Perkin–Elmer 5000 atomic absorption spectrophotometer. Crystal morphology and average size were determined by a JEOL JSM-6510 scanning electron microscope (SEM). The size and location of supported Fe species were determined by a JEOL JEM-2010 transmission electron microscope (TEM) with an acceleration voltage of 200 kV. N_2 sorption experiments were performed on a Mirae SI nanoPorosity-XG analyzer. The ^{27}Al MAS NMR spectra were measured using a Varian Inova 300 spectrometer at a spinning rate of 6.0 kHz. The operating ^{27}Al frequency was 78.156 MHz, and the spectra were obtained with an acquisition of ca. 3000 pulse transients, with a $\pi/8$ rad pulse length of 1.8 μs and a recycle delay of 0.5 s. To more clearly examine changes in the ^{27}Al resonance intensity caused by postsynthetic treatments, the amounts of zeolite samples used in ^{27}Al MAS NMR measurements were kept exactly

constant. The ^{27}Al chemical shifts are reported relative to an $Al(H_2O)_6^{3+}$ solution. The intensities of tetrahedral and octahedral resonances in each ^{27}Al MAS spectrum were calculated using Origin 8.0 curve-fitting software. NH_3 temperature-programmed desorption (TPD) was recorded on a homemade TPD instrument equipped with a thermal conductivity detector, following a procedure described elsewhere [32]. The UV–vis spectra were measured on a Shimadzu UV-2401PC spectrophotometer in diffuse reflectance mode with an integrating sphere attachment. $BaSO_4$ was used as a reference, and the spectra were transformed into the Kubelka–Munk function, $F(R)$.

The X-ray absorption fine structure (XAFS) spectra at the Fe *K*-edge were recorded on a Rigaku R-XAS instrument operating at 40 kV and 60 mA with a W filament, using self-supporting zeolite wafers 13 mm in diameter. A Ge(220) single crystal was utilized to monochromatize the white X-ray, and the XAFS spectra were taken at room temperature by a sealed photon counter with Ar at the Fe *K*-edge (7124 eV). The dwell time for each point in the data was 100 s. The spectra were analyzed using the IFEFFIT suite of programs, including Athena and Artemis [33]. The threshold energy (E_0) for all the spectra was taken as the first inflection point in the absorption edge region. The background was removed using a new method proposed by Newville et al. [34], in which low-*r* background components in the Fourier transform were minimized by comparing them with either the theoretical standard or the experimental standard containing a correct background. After the XAFS oscillation was normalized to an edge jump, the background was removed to obtain $\chi(k)$. The $\chi(k)$ in the range $2.0 \leqslant k \leqslant 12$ Å^{-1} was k^2-weighted and then Fourier transformed. While the number of independent parameters defined by the Nyquist theorem in the ranges $1.2 \leqslant k \leqslant 12$ Å^{-1} and $1.4 \leqslant r \leqslant 3.8$ Å was 15, that of variables during the curve fitting was 11, in order to make the fitting more statistically meaningful.

During the curve fitting in *q*-space after the inverse Fourier transformation, the back-scattering amplitude ($F_i(k)$), total phase shift ($\phi_i(k)$), and photoelectron mean path ($\lambda(k)$) were theoretically calculated for hematite (α-Fe_2O_3) using an *ab initio* XAFS code, FEFF6. At the outset, an overall many-body reduction factor $\left(S_0^2\right)$ of 0.74 ± 0.1 was selected for Fe, because the *bcc* Fe foil was used as an external standard. However, the first shell of this Fe standard was found to overlap with two peaks at 2.49 and 2.87 Å, which caused a large error due to the significant statistical disorder. Such peak overlaps have not been reported for other metals such as Pt, Pd, and Ir with *fcc* and/or *hcp* structures yet, the S_0^2 values of which are in the range 0.8–1.0 and are consistent with theoretical estimations [35–38]. An S_0^2 value of 0.8 was simply selected for the Fe adsorbers in zeolite samples prepared here. For the multishell fitting of framework or extra-framework Fe, on the other hand, only the first shell at 1.8–2.0 Å was initially fitted with ΔE_0 in the limited region up to 2.5 Å. Then the fitting range was gradually increased to include the multishell while considering the obtained structural parameters of the first shell as initial set values, which allowed us to obtain all initial values for the multishell. In the final curve fit, all the structural parameters including those of the first shell were considered as free fitting parameters where the Nyquist theorem was satisfied.

Electron spin resonance (ESR) spectra were measured at room temperature on a JEOL JES-FA200 spectrometer at the X-band (9.17 GHz) with a field modulation of 100 kHz and a sweep time of 10 min. Before ESR measurements, the samples were heated under vacuum to a residual pressure of 10^{-3} Torr inside a quartz tube at 100 °C for 2 h to remove the gas-phase oxygen. The packing height of zeolite particles in the tube was kept constant in all cases, with the center of the sample placed in the middle of the ESR cavity, to obtain maximum accuracy of the signals. The *g* values were determined by comparing the resonance field with that of the 2,2-diphenyl-1-picrylhydrazyl (DPPH) radical at $g = 2.0036$.

3. Results and discussion

3.1. Synthesis

Table 1 lists the results from syntheses performed using 1,4-MPB or 1,5-MPP as an organic SDA under the conditions described above. The synthesis of aluminosilicate TNU-9, TNU-10, and IM-5 zeolites in the presence of such a flexible diquaternary cation is reported to be possible only from aluminosilicate gels with a very narrow range of both SiO_2/Al_2O_3 and Na_2O/SiO_2 ratios [25–29]. Thus, our initial attempts to obtain their Fe-substituted analogs were made to by carrying out the synthesis under conditions identical to those for aluminosilicate counterparts except that $Al(NO_3)_3{\cdot}9H_2O$ was replaced by the equivalent amount of $Fe(NO_3)_3{\cdot}9H_2O$. As seen in Table 1, however, quartz or an impure zeolite was the phase formed after heating at 160 °C for 14 days. This led us to reduce the amount of $Fe(NO_3)_3{\cdot}9H_2O$ in the synthesis mixture while keeping the $SiO_2/(Fe_2O_3 + Al_2O_3)$ ratio at 60. When two-thirds of $Fe(NO_3)_3{\cdot}9H_2O$ was replaced by $Al(NO_3)_3{\cdot}9H_2O$, it was possible to crystallize pure Fe-substituted TNU-9 from the synthesis mixture with $Na_2O/SiO_2 = 0.37$ containing 1,4-MPB as an organic SDA. The synthetic results in Table 1 reveal that the $Fe_2O_3/(Fe_2O_3 + Al_2O_3)$ ratio (0.16) leading to the successful formation of Fe-substituted TNU-10 is lower than the ratio (0.34) directing the synthesis of Fe-substituted TNU-9. Also, the crystallization of Fe-substituted IM-5 in the presence of 1,5-MPP as an organic SDA was found to be practicable from synthesis mixtures with a wider range (0–0.66) of $Fe_2O_3/(Fe_2O_3 + Al_2O_3)$ ratios. As in the cases of TNU-9 and TNU-10, however, we were not able to obtain a pure IM-5 phase without adding a certain amount of Al into the synthesis mixtures. This suggests that Al plays a cooperative structure-directing role in the crystallization of the iron-substituted analogs of these three medium-pore zeolites in the presence of a particular diquaternary ammonium ion and Na^+, whereas Fe does not.

Elemental analysis indicates that the Fe content (1.7 wt%) of Fe-substituted TNU-9 synthesized using a ferrialuminosilicate gel with $Fe_2O_3/(Fe_2O_3 + Al_2O_3) = 0.34$ is not much larger than that (1.3 wt%) of Fe-substituted TNU-10 crystallized from the gel with $Fe_2O_3/(Fe_2O_3 + Al_2O_3) = 0.16$. This is not unexpected, because the typical SiO_2/Al_2O_3 ratio (14) of aluminosilicate TNU-9 is considerably higher than that (40) of aluminosilicate TNU-10 [26,27]. We also note that the Fe content (1.6 wt%) of Fe-substituted IM-5 obtained from a synthesis mixture with $Fe_2O_3/(Fe_2O_3 + Al_2O_3) = 0.34$ is marginally smaller than that (1.7 wt%) of Fe-substituted TNU-9 from a synthesis mixture with an identical oxide composition except that a different organic SDA (1,5-MPB) was used. Due to the similarity in their Fe content (1.5 ± 0.2 wt%), therefore, we will use these three zeolites as catalysts for direct N_2O decomposition in order to understand the role of zeolite structure in the decomposition activity of zeolite-supported Fe catalysts. For convenience's sake, we will refer to them simply as Fe-TNU-9, Fe-TNU-10, and Fe-IM-5, respectively, although they contains both Fe and Al atoms in framework positions (Table 2).

3.2. Catalytic activity

Fig. 1 shows N_2O conversion as a function of reaction temperature in N_2O decomposition over the proton and steam-activated forms of Fe-TNU-9(HS), Fe-TNU-10(HS), and Fe-IM-5(HS) at 1000 ppm N_2O and 4% O_2 in the feed, with or without 10% H_2O

Table 1
Syntheses from gel composition $4.5R{\cdot}xNa_2O{\cdot}yFe_2O_3{\cdot}(0.5-y)Al_2O_3{\cdot}30SiO_2{\cdot}1200H_2O$.[a]

y	R = 1,4-MPB		R = 1,5-MPP
	x = 11.0	x = 15.0	x = 11.0
	Product[b]	Product[b]	Product[b]
0.50	Quartz	Quartz	Fe-IM-5 + L[c] + quartz
0.33	Quartz + Fe-NU-87	Analcime	Fe-IM-5
0.17	Fe-TNU-9	Fe-TNU-10 + Fe-NU-87	Fe-IM-5
0.08	Fe-TNU-9 + Fe-MCM-22(P)	Fe-TNU-10	Fe-IM-5
0	Al-TNU-9	Al-TNU-10	Al-IM-5

[a] Crystallization was performed under rotation (100 rpm) at 160 °C for 14 days.
[b] The product appearing first is the major phase.
[c] Unknown, probably layered phase.

Table 2
Physical properties of the representative iron zeolites prepared in this study.

Zeolite	IZA Code	Si/Al[a]	Fe (wt.%)[a]	Si/Fe[a]	Fe/Al[a]	Crystal shape and average size[b] (μm)	BET surface area[c] ($m^2\ g^{-1}$)		
							Total	Microporous	External
Fe-TNU-9(HS)	TUN	21	1.71	42	0.50	Rods, 0.3 × 0.8	545 (481)	477 (413)	68 (68)
Fe-TNU-10(HS)	STI	11	1.29	56	0.20	Rectangular platelets, 0.5 × 1.0 × 0.1	477 (440)	409 (369)	68 (71)
Fe-IM-5(HS)	IMF	22	1.64	45	0.49	Rods, 0.1 × 0.3	422 (372)	348 (298)	74 (74)
Fe-ZSM-5(HS)	MFI	36	1.41	57	0.63	Spherulites, 4	516 (358)	411 (262)	106 (96)
Fe-TNU-9(S)	TUN	17	5.35	–		Rods, 0.3 × 0.8	417 (394)	359 (340)	58 (54)
Fe-ZSM-5(S)	MFI	29	3.57	–		Spherulites, 1	386 (374)	316 (310)	70 (64)

[a] Determined by elemental analysis.
[b] Determined by SEM.
[c] Determined from N_2 sorption data for the proton form of each sample. The values in parentheses are those determined from the steamed zeolites.

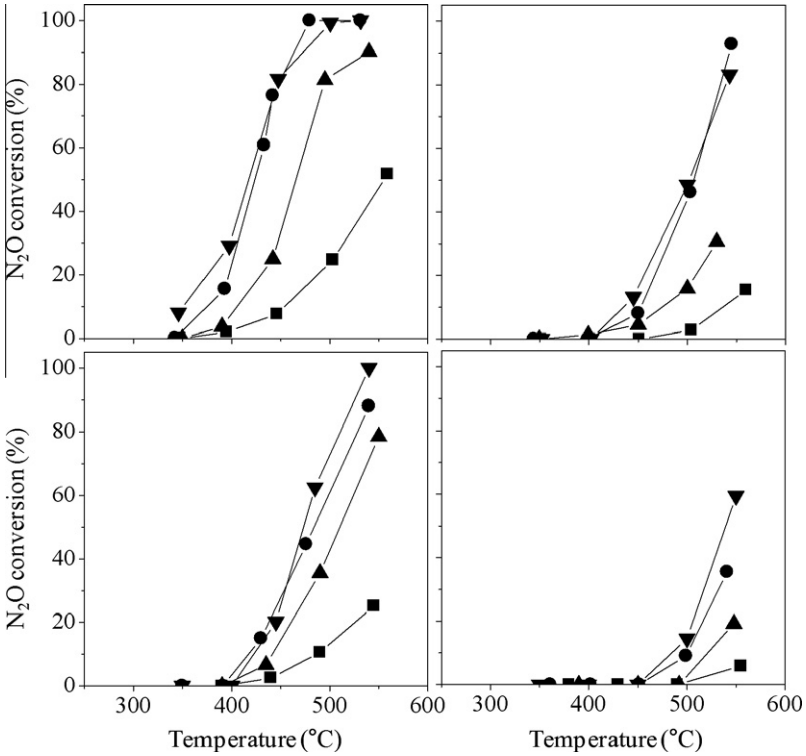

Fig. 1. N_2O conversion as a function of temperature in N_2O decomposition over the proton (bottom) and steam-activated (top) forms of isomorphously Fe-substituted zeolites with different framework topologies under dry (left) and wet (right) feeds: ●, Fe-TNU-9(HS); ■, Fe-TNU-10(HS); ▲, Fe-IM-5(HS); ▼, Fe-ZSM-5(HS). The reactions were run with a feed containing 1000 ppm N_2O and 4% O_2 in N_2 balance, with/without 10% H_2O present, at 42,000 h^{-1} GHSV.

present. For comparison, the catalytic results for the corresponding forms of Fe-ZSM-5(HS) with a similar Fe content (1.4 wt%) are also given in Fig. 1. It can be seen that the decomposition activity in both the absence and presence of H_2O is higher in the order H–Fe-TNU-10(HS) < H–Fe-IM-5(HS) < H–Fe-TNU-9(HS) ⩽ H–Fe-ZSM-5(HS), which is also the case for the steamed analogs. On the other hand, steaming is known to yield a notable increase in the decomposition activity of isomorphously iron-substituted zeolites

[16,24,39,40]. This can be further evidenced by their specific activities for N_2O decomposition per mole of Fe ions (turnover frequencies, TOFs), listed in Table 3. At 500 °C under dry conditions, for example, the TOF value of *s*-Fe-TNU-9(HS) is approximately 1.6 times higher than that of H–Fe-TNU-9(HS). In contrast, steaming yielded no significant changes in the TOF value of Fe-TNU-9(S) and Fe-ZSM-5(S), iron zeolites prepared by the $FeCl_3$ sublimation method. This indicates that the nature and distribution of extra-framework iron species and hence their decomposition activity differ notably according to the type of preparation method, in good agreement with previous studies [16,24,39,41].

One strong point of Fe-ZSM-5 as an N_2O decomposition catalyst compared to other catalysts, especially to noble metal-based ones, is the enhancement of its decomposition activity by the presence of a small amount of NO in the feed [16,39,42]. To check whether this promotion effect is also valid for other structure types of iron zeolites, therefore, the N_2O decomposition activities of the proton and steam-activated forms of iron-substituted zeolites with four different framework structures at 1000 ppm N_2O, 200 ppm NO, and 4% O_2 in the feed have been measured. As can be seen in Supplementary Fig. S1, addition of 200 ppm ($NO/N_2O = 0.2$) NO noticeably enhances the reaction rates of all these iron zeolites. To accurately quantify the extent of increase in decomposition activity, the TOF values of the proton and steam-activated forms of Fe-TNU-9(HS), Fe-TNU-10(HS), Fe-IM-5(HS), and Fe-ZSM-5(HS) at 450 °C in the absence or presence of 200 ppm NO have been calculated and are given in Table 4. We should note here that the values of *s*-Fe-TNU-9(HS) and *s*-Fe-ZSM-5(HS) are calculated from the catalytic results obtained at 400 °C, because they easily yielded 100% N_2O conversion upon addition of NO to the feed at 450 °C (Supplementary Fig. S1). The TOF data in Table 4 reveal that the extent of increase in TOF value with NO addition is not the same for the proton form of all four iron zeolites with different framework topologies. This is also the case of their steam-activated form. Such differences in the promotion effect suggest that the type of extra-framework iron species formed during the calcination and steaming steps is significantly altered according to the zeolite support structure, giving different decomposition activities.

3.3. Characterization

The powder XRD patterns of the steam-activated forms of Fe-TNU-9(HS), Fe-TNU-10(HS), Fe-IM-5(HS), and Fe-ZSM-5(HS) match well with the patterns of their as-made forms, as well as with those of aluminosilicate counterparts, except for minor changes in the relative X-ray peak intensity and position (Supplementary Fig. S2). This indicates that the Fe-substituted zeolites with different framework structures prepared here maintain their structures during the initial calcinations at 550 °C to remove the organic SDAs occluded and the subsequent NH_4^+ ion-exchange, recalcination, and steaming steps, which is further supported by the N_2 adsorption data in Table 2. The absence of reflections other than those not only from these zeolites but also from α-Fe_2O_3 suggests that the extra-framework iron oxide particles generated by the extraction of framework Fe atoms during the calcination and/or steaming are small enough to be below the detection limit of powder XRD. Since no noticeable increase in external surface area of zeolites was found even after steaming at 600 °C (Table 2), in addition, it appears that the formation of mesopores in steamed zeolites is negligible.

Table 3
Turnover frequencies of various iron zeolites for N_2O decomposition determined at 500 °C and 42,000 h^{-1} GHSV after 1 h on stream.

Catalyst	TOF ($\times 10^{-4}$ s^{-1})[a]			
	H- or as-made form		Steam-activated form	
	w/o water	w/ water	w/o water	w/ water
Fe-TNU-9(HS)	18.7	3.0	30.6	13.5
Fe-TNU-10(HS)	5.4	0.4	9.7	1.1
Fe-IM-5(HS)	13.7	0.9	26.3	5.1
Fe-ZSM-5(HS)	27.0	5.4	36.8	18.0
Fe-TNU-9(S)	8.8	3.8	9.7	3.8
Fe-ZSM-5(S)	13.2	4.8	14.0	4.8

[a] Moles of N_2O converted per mole of Fe ions per s. Feed composition: 1000 ppm N_2O and 4% O_2 in N_2 balance, with or without 10% H_2O present.

Table 4
TOF values of the proton and steam-activated forms of four iron-substituted zeolites with different framework topologies for N_2O decomposition determined at 450 °C and 42,000 h^{-1} GHSV, with or without 200 ppm NO present in the feed, after 1 h on stream.[a]

Catalyst	TOF ($\times 10^{-4}$ s^{-1})					
	Proton form			Steam-activated form		
	w/o NO	w/ NO	ε[b]	w/o NO	w/ NO	ε[b]
Fe-TNU-9(HS)	8.3	19.0	1.3	6.4[c]	20.2[c]	2.2[c]
Fe-TNU-10(HS)	1.4	2.8	1.0	3.3	7.7	1.3
Fe-IM-5(HS)	4.0	13.9	2.5	10.2	23.9	1.3
Fe-ZSM-5(HS)	8.9	29.0	2.3	11.9[c]	31.6[c]	1.7[c]

[a] Feed composition: 1000 ppm N_2O and 4% O_2 in N_2 balance.
[b] Extent of TOF enhancement by NO addition defined as $(TOF_{w/} - TOF_{w/o})/TOF_{w/o}$, where $TOF_{w/}$ and $TOF_{w/o}$ are the turnover frequencies determined in the presence and absence of 200 ppm NO, respectively.
[c] TOF values determined at 400 °C, because N_2O conversion at 450 °C reaches 100% upon addition of NO to the feed.

When converted into their proton form, all as-made Fe-substituted zeolites showed a color change from white to pale brown, indicative of the extraction of a portion of tetrahedral Fe atoms from their framework positions during the calcination and exchange steps. Unlike the proton form of the other three zeolites, however, H–Fe-TNU-10(HS) underwent no further color change to dark brown after steaming, despite the similarity in their Fe content (Table 2). This suggests that the thermal stability of framework Fe atoms may differ according to the type of zeolite structure into which this trivalent heteroatom has been incorporated. Spectroscopic evidence to support this speculation will be given below.

Fig. 2 shows the ^{27}Al MAS NMR spectra of the as-made, proton, and steam-activated forms of four iron-substituted zeolites with different framework structures. Here, the heights of the most intense ^{27}Al resonance around 55 ppm, typical of framework Al atoms, from each of the as-made zeolites were adjusted on a similar scale in order to display more clearly the spectral changes caused by calcination and steam activation. Table 5 gives the degrees of dealumination and the Si/Al_F and Fe/Al_{EF} ratios of their proton and steam-activated forms determined from ^{27}Al MAS NMR data in Fig. 2, where Al_F and Al_{EF} are the framework and extra-framework Al atoms, respectively. These data clearly show that the degree of dealumination (i.e., the thermal stability of framework Al atoms) of zeolites due to calcination or steam activation varies notably with the zeolite topology, as previously reported [43,44]. Compared with that from the other three as-made iron zeolites, in particular, the resonance at 55 ppm from *am*-Fe-TNU-10(HS) was found to give a considerably more severe decrease in intensity, suggesting the lower thermal stability of its framework Al atoms.

It has been proposed repeatedly that the catalytically active sites for N_2O decomposition, as well as for benzene hydroxylation with N_2O, are formed by a combination of extra-framework Fe and Al species [40,45–48]. Sun et al. have shown that the decomposition activity of Fe-ZSM-5(S) increases with increasing extra-framework Al content [45]. As seen in Table 5, however, both proton and

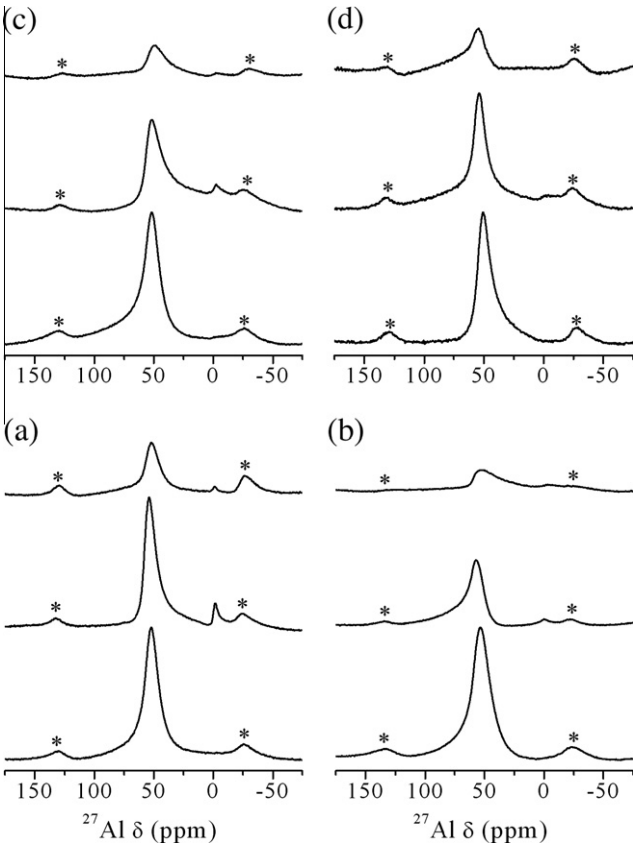

Fig. 2. ^{27}Al MAS NMR spectra of the as-made (bottom), proton (middle), and steam-activated (top) forms of: (a) Fe-TNU-9(HS), (b) Fe-TNU-10(HS), (c) Fe-IM-5(HS), and (d) Fe-ZSM-5(HS). Spinning sidebands are marked by asterisks.

Table 5
Degrees of dealumination and Si/Al_F and Fe/Al_{EF} ratios of the proton and steam-activated forms of iron-substituted zeolites with different framework topologies determined from ^{27}Al MAS NMR data.

Catalyst	Proton form			Steam-activated form		
	δ_{deAl}[a] (%)	Si/Al_F[b]	Fe/Al_{EF}[b]	δ_{deAl}[a] (%)	Si/Al_F[b]	Fe/Al_{EF}[b]
Fe-TNU-9(HS)	15	25 (21)	3.33	58	50	0.86
Fe-TNU-10(HS)	58	26 (11)	0.34	84	69	0.23
Fe-IM-5(HS)	34	33 (22)	1.43	70	73	0.69
Fe-ZSM-5(HS)	18	44 (36)	3.57	64	100	0.99

[a] Degree of dealumination defined as $\{1 - (I_{55,H}$ or $I_{55,s})/I_{55,am}\} \times 100$, where $I_{55,H}$, $I_{55,s}$, and $I_{55,am}$ are the intensities of the tetrahedral ^{27}Al NMR resonance appearing around 55 ppm from the proton, steam-activated, and as-made forms of each iron zeolite.

[b] Determined by a combination of elemental analysis and ^{27}Al MAS NMR data. Al_F and Al_{EF} indicate the framework and extra-framework Al atoms, respectively. The framework Si/Al ratios in parentheses are the same as the values in Table 2.

steam-activated forms of Fe-TNU-10(HS), the activities of which are much lower than those of the corresponding forms of the other three iron-substituted zeolites (Table 3), are characterized by significantly lower Fe/Al_{EF} ratios. Therefore, we speculate that the influence of zeolite structure on the N_2O decomposition activity of supported iron catalysts may be stronger than that of Fe/Al_{EF} ratio or extra-framework Al content.

Fig. 3 shows the NH_3 TPD profiles obtained from the proton forms of isomorphously substituted iron zeolites with four different framework topologies and their steamed analogs. The profiles from the as-made and steam-activated forms of Fe-TNU-9(S) and Fe-ZSM-5(S) zeolites are also given in Fig. 3. It can be seen that

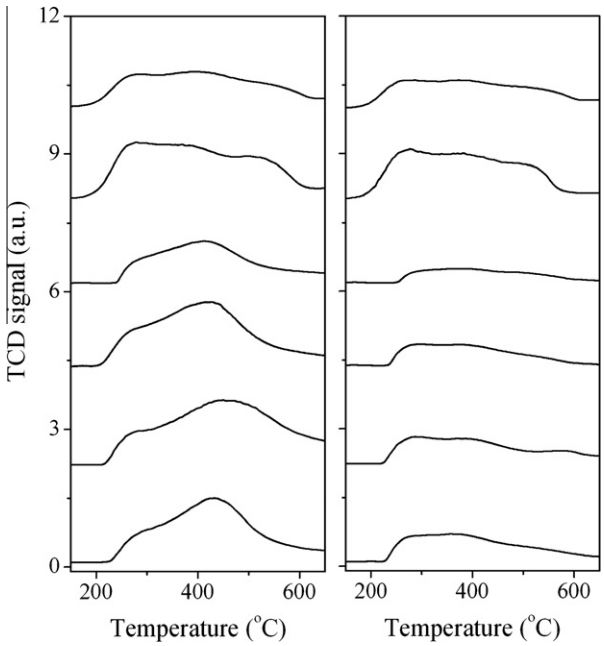

Fig. 3. NH_3 TPD profiles of the proton or as-made (left) and steamed-activated (right) forms of (from bottom to top) Fe-TNU-9(HS), Fe-TNU-10(HS), Fe-IM-5(HS), Fe-ZSM-5(HS), Fe-TNU-9(S), and Fe-ZSM-5(S).

the high-temperature desorption peak from H–Fe-TNU-10(HS) is located at a slightly higher temperature (maximum around 460 °C) than for the proton forms of the other three zeolites. This indicates that the strong acid sites in the former zeolite possess a slightly higher strength than those in the latter ones. As expected from their trivalent heteroatom contents (Table 2), in addition, the total areas of NH_3 desorption (i.e., the densities of acid sites) from H–Fe-TNU-10(HS) and H–Fe-ZSM-5(HS) were found to be somewhat larger and smaller than those from H–Fe-TNU-9(HS) and H–Fe-IM-5(HS), respectively. Unlike those prepared by sublimation, however, the iron zeolites obtained by hydrothermal synthesis show a notable decrease in both the strength and density of acid sites upon steaming. This suggests that most of the acid sites in the proton form originates from the presence of both Al and Fe in framework positions. In addition, it can be concluded from similarities in the Al content (Table 2) that the degree of dealumination is considerably higher in iron zeolites containing both framework Al and Fe atoms than in those giving framework Al atoms only.

Fig. 4 shows the TEM micrographs of a series of iron zeolites prepared in this study. No detectable dots or particles can be observed in the crystals of any as-made iron-substituted materials. However, there are very small particles with diameter ca. 0.5–1 nm in the micrographs of their proton forms, indicating the extraction of a portion of framework Fe atoms to extra-framework positions. As expected, in addition, steam activation removes framework Fe atoms in a severer manner, generating homogenously dispersed iron oxide particles with diameter 1–2 nm. It is worth noting that both the number and size of particles are somewhat smaller in *s*-Fe-TNU-10(HS) than in the steam-activated forms of the other three iron-substituted zeolites, which can be attributed either to a higher thermal stability of framework Fe atoms in the former zeolite or to a lower tendency of its extra-framework iron species to form large iron oxide particles. Further characterization to address this issue will be given below. No detectable changes in the number and size of particles were found in the TEM micrographs of *am*-Fe-TNU-9(S) and *s*-Fe-TNU-9(S). As seen in Fig. 4, however,

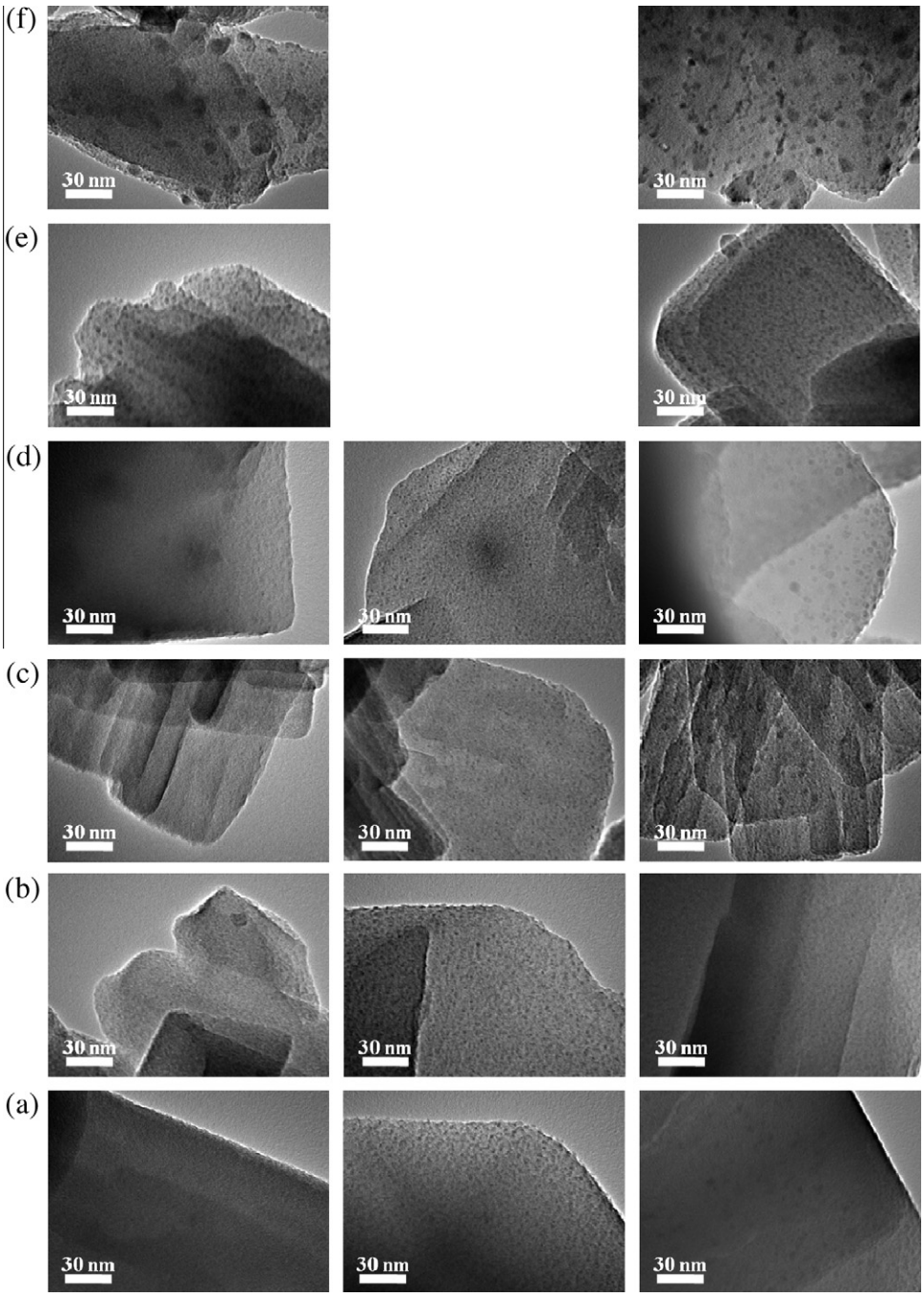

Fig. 4. TEM micrographs of the as-made (left), proton (middle), and steam-activated (right) forms of: (a) Fe-TNU-9(HS), (b) Fe-TNU-10(HS), (c) Fe-IM-5(HS), (d) Fe-ZSM-5(HS), (e) Fe-TNU-9(S), and (f) Fe-ZSM-5(S).

the micrographs of *am*-Fe-ZSM-5(S) and *s*-Fe-ZSM-5(S) are characterized by much larger particles of 3–15 nm that are inactive for N_2O decomposition [7,16,24,39]. In addition, the fact that the latter ZSM-5 material has a considerably larger number of particles suggests that the agglomeration of iron oxide clusters by steaming is more severe in ZSM-5 than in TNU-9.

Fig. 5 shows the UV–vis spectra of the as-made, proton, and steam-activated forms of iron zeolites with different framework structures. The spectra of the as-made forms of all four iron-substituted zeolites are dominated by intense $Fe^{3+} \leftarrow O$ charge-transfer (CT) bands centered at $\leqslant$250 nm that can be attributed to the isolated framework Fe^{3+} ions [37,49,50]. As seen in Fig. 5, however, the spectra of H–Fe-TNU-9(HS) and H–Fe-IM-5(HS) exhibit a broad contribution between 300 and 400 nm, assignable to octahedral Fe^{3+} ions in small oligonuclear $Fe_x^{3+}O_y$ clusters formed within zeolite micropores. The presence of a broad contribution above 400 nm in the spectrum of H–Fe-ZSM-5(HS) indicates the formation of larger Fe_2O_3 particles during the calcination and exchange steps, which is in contrast to the TEM results in Fig. 4. Thus, the number of Fe_2O_3 particles in this zeolite might not be large enough to be easily observed by TEM. It is also remarkable that a contribution above 400 nm is observable in the UV–vis spectra of all steamed samples. This clearly shows that steaming of the proton form of iron-substituted zeolites results in further Fe extraction from their frameworks, as well as an increased degree of iron clustering. Of particular interest is the spectrum of *s*-Fe-TNU-10(HS), in

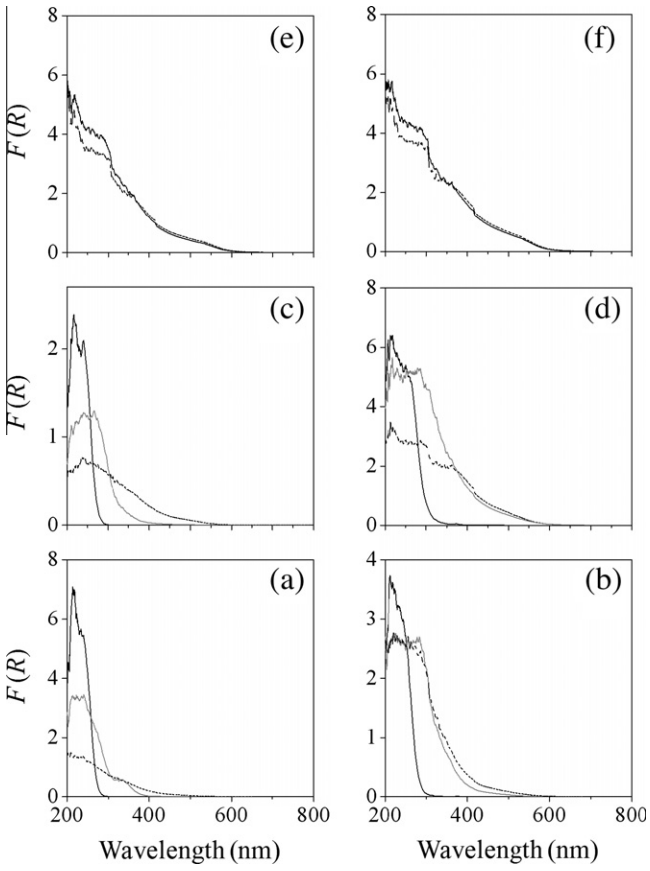

Fig. 5. UV–vis spectra of the as-made (solid line), proton (gray line), and steam-activated (dotted line) forms of: (a) Fe-TNU-9(HS), (b) Fe-TNU-10(HS), (c) Fe-IM-5(HS), (d) Fe-ZSM-5(HS), (e) Fe-TNU-9(S), and (f) Fe-ZSM-5(S).

which the intensities of CT transition bands between 200 and 300 nm are nearly the same as those observed for the spectrum of its proton form. This suggests that the nature and distribution of iron species in Fe-TNU-10(HS) have not been much modified even after steam activation at 600 °C. Unlike the case of the other three iron-substituted zeolites, therefore, a fraction of framework Fe atoms in this STI-type zeolite appears to be thermally stable enough to stand such a severe treatment.

The UV–vis spectra of *am*-Fe-TNU-9(S) and *am*-Fe-ZSM-5(S) show much broader, almost featureless bands in the region below 600 nm, indicating the presence of various iron species ranging from isolated Fe^{3+} ions to large Fe_2O_3 particles in these two zeolites prepared by the $FeCl_3$ sublimation method. We also note that the intensities of the CT bands from *am*-Fe-ZSM-5(S) are similar to those observed for *am*-Fe-TNU-9(S). As seen in Fig. 5, however, the intensities of *d*–*d* transition bands appearing at 350–600 nm are slightly higher in the spectrum of the former zeolite. This suggests the formation of larger Fe_2O_3 particles in *am*-Fe-ZSM-5(S). Although steam treatment of these two zeolites brings out no noticeable changes in *d*–*d* transition band intensity, there is a slight decrease in their CT band intensity. Therefore, it is most likely that no significant agglomeration of iron oxide clusters has taken place during steaming, which matches well the TEM results in Fig. 4.

Fig. 6 shows the k^2-weighted XAFS Fourier transforms of the as-made, proton, and steam-activated forms of Fe-TNU-9(HS), Fe-TNU-10(HS), Fe-IM-5(HS), and Fe-ZSM-5(HS) at the Fe *K*-edge, together with the Fourier transforms of the as-made and steam-activated forms of Fe-TNU-9(S) and Fe-ZSM-5(S). We note that the best-fitted radial distribution function of each Fourier transform is in good agreement with its experimental XAFS spectrum. Tables 6 and 7 list the structural parameters determined through multishell curve fitting for their XAFS spectra. Besides α-Fe_2O_3, Fe-TNU-10(HS) with the STI topology was also used in generating the theoretical standard for tetrahedral Fe atoms in the zeolite framework. The structural parameter data reveal that unlike the as-made forms of the other three iron-substituted zeolites, *am*-Fe-TNU-10(HS) possesses octahedral Fe in the Fe–O bond with a bond distance (*R*) of 1.8 Å, together with a non-negligible contribution of multiple scattering corresponding to the Fe–O–Si–O–Fe and Fe–Si–Fe paths with *R* = 3.3 Å. Among the four crystallographically different tetrahedral sites (T-sites) in the STI topology, site T2, with a multiplicity of 16, interlinks two layers, so that it has much less acute T-O-T angles than the other three T-sites [27,51]. Thus, if Fe atoms in the TNU-10 structure preferentially occupied site T2, water molecules could easily be adsorbed onto the framework Fe atoms, allowing them to be in an octahedral environment. Thus, the XAFS data on *am*-Fe-TNU-10(HS) could be considered as experimental evidence for the non-random nature of Fe substitution in STI-type zeolites.

The XAFS Fourier transforms in Fig. 6 also show that the proton forms of all four isomorphously iron-substituted zeolites exhibit an Fe–Fe bond with *R* = 2.3 Å, characteristic of α-Fe_2O_3, as well as an Fe–O bond with *R* = 2.0 Å. It is thus clear that the extraction of a portion of the framework Fe atoms to extra-framework positions, followed by the formation of small oligonuclear $Fe_x^{3+}O_y$ clusters, occurred during the calcination and NH_4^+ exchange steps. On the other hand, comparison of the XAFS data on steam-activated zeolites reveals that the degree of extraction of framework Fe atoms can be altered according to the structure type of zeolites. As seen in Fig. 6, the relative intensity of the Fe–O peak with *R* = 2.0 Å due to framework Fe atoms in the Fourier transform becomes higher in the order *s*-Fe-TNU-9(HS) ≪ *s*-Fe-ZSM-5(HS) ∼ *s*-Fe-IM-5(HS) < *s*-Fe-TNU-10(HS). The highest degree of extraction of framework Fe in *s*-Fe-TNU-9(HS) can be further evidenced by the fact that the coordination number (CN) of its Fe in the Fe–Fe bond with *R* = 2.2 Å is 3.4, which is much larger than the CN values of Fe in the corresponding bond for the steam-activated forms of the other three iron-substituted zeolites (Table 7). These XAFS results can be correlated with the very poor N_2O decomposition activity of Fe-TNU-10(HS), because the Fe atoms in zeolite framework positions are not catalytically active for this reaction [16].

Analysis of the spectra of *am*-Fe-TNU-9(S) and *am*-Fe-ZSM-5(S) reveals the existence of one Fe–O shell with *R* = 2.0 Å and two Fe–Fe shells with bond distances greater than 2.0 Å. We note here that the CN values (4.1 and 3.4, respectively) of their Fe atoms in the Fe–O bond with *R* = 2.0 Å and in the Fe–Fe bond with *R* = 3.0 Å are not very different from those (4 and 2, respectively) of Fe in the corresponding bonds for the α-Fe_2O_3 lattice, suggesting the formation of large iron oxide particles, as already evidenced by the TEM results in Fig. 4. In contrast, the CN values (3.9 and 6.0, respectively) of Fe in the Fe–Fe bond with *R* = 3.0 Å for *s*-Fe-TNU-9(S) and *s*-Fe-ZSM-5(S) are considerably larger than those (1.7 and 2.0, respectively) of Fe in the same bond for their as-made form (Tables 6 and 7). This indicates that steaming results in further sintering of Fe_2O_3 nanoparticles. Also, there is a large contribution of multiple scattering corresponding to the Fe–Fe(Si) path with *R* = 3.3 Å, within experimental error. It thus appears that the Fe^{3+} ions sublimed into the TNU-9 and ZSM-5 zeolite crystals are further spread or dispersed during steam activation, maximizing the surface contact and hence the multiple scattering contribution.

Fig. 7 shows the ESR spectra of the as-made, proton, and steam-activated forms of all iron zeolites prepared here. The spectra of *am*-Fe-TNU-9(HS), *am*-Fe-TNU-10(HS), *am*-Fe-IM-5(HS), and *am*-Fe-ZSM-5(HS) are characterized by almost identical line shapes in which two signals appear at effective *g* values of 2.0 and 4.2.

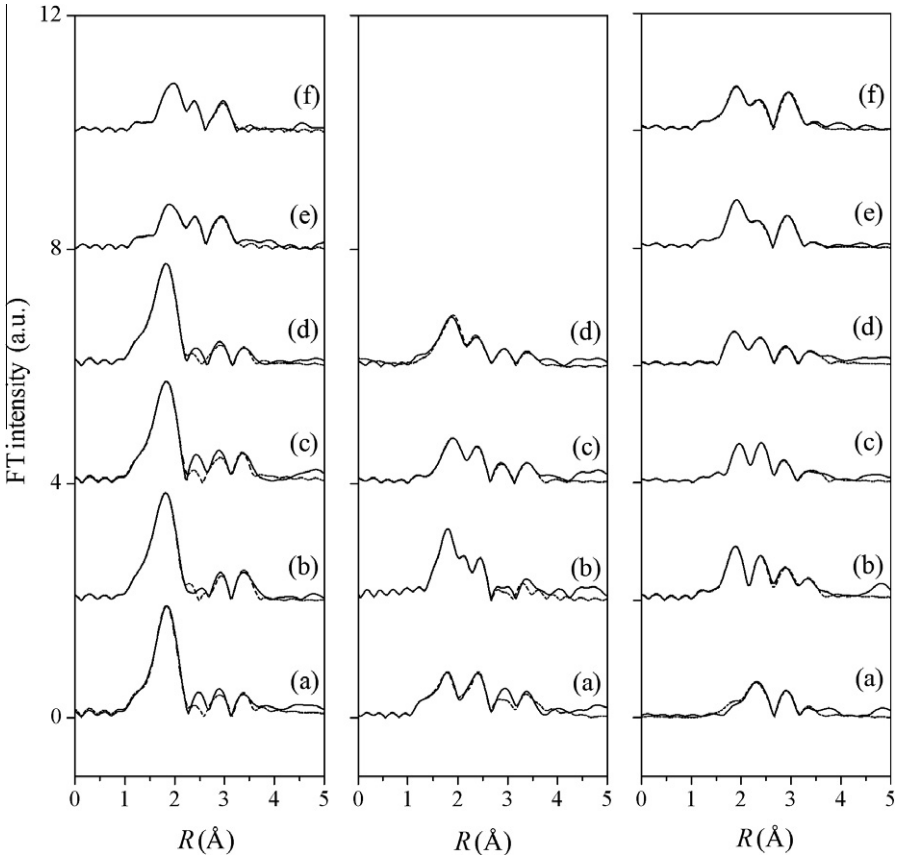

Fig. 6. XAFS Fourier transforms of the as-made (left), proton (middle), and steam-activated (right) forms of: (a) Fe-TNU-9(HS), (b) Fe-TNU-10(HS), (c) Fe-IM-5(HS), (d) Fe-ZSM-5(HS), (e) Fe-TNU-9(S), and (f) Fe-ZSM-5(S) at the Fe *K*-edge. The best-fitted function of each Fourier transform is given as a dotted line.

Because the UV–vis spectra of these Fe-substituted zeolites in the as-made form verify the presence of isolated, tetrahedral Fe^{3+} ions only (Fig. 5), both signals at $g = 2.0$ and 4.2 can be attributed to framework Fe^{3+} ions, but under low and high distortions, respectively [31]. As repeatedly reported [41,52,53], on the other hand, the ESR spectrum of *am*-Fe-ZSM-5(S) shows a line shape quite similar to that of Fe^{3+} in α-Fe_2O_3. However, the spectrum of *am*-Fe-TNU-9(S) gives a very broad signal at a *g* value considerably lower than 4.2. This suggests the highly dispersed nature of its iron oxide particles, which is consistent with the TEM results in Fig. 4.

Although less intense, the ESR spectra of the proton forms of all iron-substituted zeolites hydrothermally synthesized here show line shapes similar to those observed for their as-made forms. Unlike the other two zeolites, however, the spectra of H–Fe-TNU-9(HS) and H–Fe-ZSM-5(HS) give more than one superimposed signal at $g = 2.0$ and/or 4.2. This reflects that the extra-framework Fe^{3+} species formed are not homogeneously distributed within the zeolite micropores. Fig. 7 also shows that the ESR spectra of the proton forms of Fe-substituted zeolites undergo a dramatic change in line shape and intensity after steaming. As a result, for example, the spectra of *s*-Fe-TNU-9(HS) and *s*-Fe-ZSM-5(HS) become similar to those of the as-made or steam-activated forms of Fe-TNU-9(S) and Fe-ZSM-5(S). In particular, the spectrum of *s*-Fe-TNU-10(HS) still shows a noticeable signal at $g = 4.2$. In line with the UV–vis and Fe *K*-edge XAFS results, therefore, it is clear that the thermal stability of zeolite framework Fe depends strongly on the type of zeolite structures into which this trivalent heteroatom has been isomorphously substituted. If this is the case, the structure type of zeolites will then be an intrinsic factor affecting the nature and distribution of extra-framework iron species generated within the zeolite micropores during the post-synthetic treatments and hence their N_2O decomposition activity.

4. Conclusions

The hydrothermal synthesis of isomorphously substituted Fe-TNU-9, Fe-TNU-10, and Fe-IM-5 zeolites containing both Fe and Al in framework positions is presented. Under the synthesis conditions studied here, we were not able to fully replace Al with Fe in the framework of these medium-pore zeolites, implying notable differences in the structure-directing ability of Al and Fe in their crystallization. The presence of a certain amount of Al in the synthesis mixture appears to be essential for promoting more stable nuclei, which can grow into crystals of Fe-TNU-9, Fe-TNU-10, or Fe-IM-5. The turnover frequency of iron-substituted zeolites for N_2O decomposition is higher in the order Fe-TNU-10 < Fe-IM-5 < Fe-TNU-9 < Fe-ZSM-5, regardless of catalyst steaming or the presence of water in the reaction stream. Interestingly, the extent of increase in turnover frequency with NO addition is not the same for their proton and steam-activated forms. Moreover, the effect of zeolite topology on the N_2O decomposition activity of supported iron catalysts is stronger than that of Fe/Al_{EF} ratio or extra-framework Al content. The overall characterization results of this study strongly suggest that the thermal stability of Fe atoms substituted into the zeolite framework is altered notably according to the structure type of zeolites, which may intrinsically influence the nature and distribution of extra-framework iron species formed during the calcination and steaming steps, and hence their N_2O decomposition activity.

Table 6
Coordination number (CN), bond distance (R), Debye–Waller parameter (σ^2), and energy shift (ΔE) of the Fe K-edge for the as-made form of iron zeolites prepared in this study.

Zeolite	Fe–O			Fe–Si			Fe–O–Si–O–Fe			Fe–Fe			Fe–Fe			ΔE (eV)	R-factor
	CN (±0.5)	R (±0.01 Å)	σ^2 ($10^{-4}\times$ Å^2)	CN (±0.5)	R (±0.01 Å)	σ^2 ($10^{-4}\times$ Å^2)	CN (±0.5)	R (±0.01 Å)	σ^2 ($10^{-4}\times$ Å^2)	CN (±0.5)	R (±0.01 Å)	σ^2 ($10^{-4}\times$ Å^2)	CN (±0.5)	R (±0.01 Å)	σ^2 ($10^{-4}\times$ Å^2)		
am-Fe-TNU-9(HS)	3.7	1.86	~0	6.1	3.17	22	7.2	3.29	~0							−2.7	0.010
am-Fe-TNU-10(HS)	6.5	1.83	39	10.8	3.21	48	13.0	3.33	27							−6.3	0.003
am-Fe-IM-5(HS)	3.2	1.85	~0	9.6	3.16	167	9.7	3.29	163							−4.3	0.012
am-Fe-ZSM-5(HS)	3.8	1.85	3	6.8	3.18	210	7.6	3.30	209							−4.7	0.004
am-Fe-TNU-9(S)	4.1	1.95	127							0.3	2.30	~0	1.7	2.96	49	−3.1	0.030
am-Fe-ZSM-5(S)	3.4	1.97	84							0.2	2.29	~0	2.0	2.98	79	0.0	0.011

Table 7
Coordination number (CN), bond distance (R), Debye–Waller parameter (σ^2), and energy shift (ΔE) of the Fe K-edge for the proton and steam-activated forms of iron-substituted zeolites.

Zeolite	Fe–O			Fe–Fe			Fe–Fe			Fe–Fe (Si)			ΔE (eV)	R-factor
	CN (±0.5)	R (±0.01 Å)	σ^2 ($10^{-4}\times$ Å^2)	CN (±0.5)	R (±0.01 Å)	σ^2 ($10^{-4}\times$ Å^2)	CN (±0.5)	R (±0.01 Å)	σ^2 ($10^{-4}\times$ Å^2)	CN (±0.5)	R (±0.01 Å)	σ^2 ($10^{-4}\times$ Å^2)		
H–Fe-TNU-9(HS)	4.0	1.93	177	1.6	2.24	86	4.7	3.00	86	4.6	3.25	93	0.1	0.044
H–Fe-TNU-10(HS)	3.7	1.98	54	1.3	2.26	88	1.6	2.98	39	3.0	3.18	88	−2.4	0.011
H–Fe-IM-5(HS)	4.3	1.97	115	0.7	2.26	46	5.2	3.03	164	2.2	3.26	46	0.0	0.014
H–Fe-ZSM-5(HS)	3.8	1.93	122	0.7	2.29	65	11.1	3.06	320	0.7	3.28	8	−1.0	0.023
s-Fe-TNU-9(HS)	1.2	1.93	74	3.4	2.23	189	5.7	2.99	137	2.1	3.22	65	−2.0	0.021
s-Fe-TNU-10(HS)	2.3	1.93	61	1.5	2.23	83	2.3	2.97	27	3.3	3.22	83	−1.0	0.023
s-Fe-IM-5(HS)	2.0	2.03	38	0.4	2.28	~0	1.9	3.02	62	0.7	3.22	~0	2.3	0.025
s-Fe-ZSM-5(HS)	3.6	2.00	156	0.2	2.28	~0	2.6	3.05	128	0.6	3.27	~0	0.5	0.022
s-Fe-TNU-9(S)	2.2	1.94	38	3.1	2.22	243	3.9	2.98	96	7.0	3.23	243	−0.7	0.077
s-Fe-ZSM-5(S)	2.9	1.95	66	1.7	2.24	140	6.0	3.01	113	4.3	3.27	140	0.0	0.070

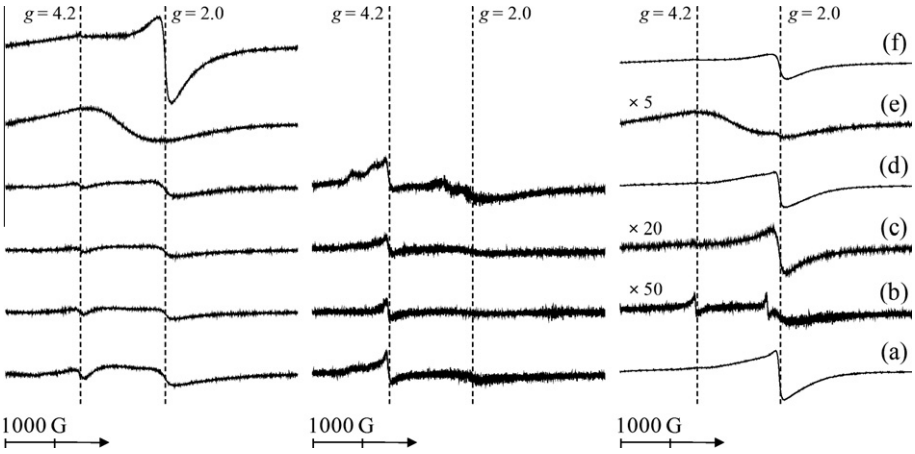

Fig. 7. ESR spectra of the as-made (left), proton (middle), and steam-activated (right) forms of (a) Fe-TNU-9(HS), (b) Fe-TNU-10(HS), (c) Fe-IM-5(HS), (d) Fe-ZSM-5(HS), (e) Fe-TNU-9(S), and (f) Fe-ZSM-5(S).

Acknowledgment

This work was supported by the National Research Foundation of Korea (R0A-2007-000-20050-9 and 2011-0029806).

Appendix A. Supplementary material

Supplementary data associated with this article can be found, in the online version, at doi:10.1016/j.jcat.2011.08.012.

References

[1] Kyoto Protocol to the United Nations Framework Convention on Climate Change, Annex A, Kyoto, Japan, December 1997. <http://unfccc.int/resource/docs/convkp/kpeng.pdf>.
[2] H. Rodhe, Science 248 (1990) 1217.
[3] K. Sun, H. Xia, E.J.M. Hensen, R.A. van Santen, C. Li, J. Catal. 238 (2006) 186.
[4] J.T. Houghton et al. (Eds.), Climate Change 2001, The Scientific Basis, Contribution of the Working Group I to the Third Assessment Report of the IPCC, Cambridge, 2001.
[5] R.W. van der Brink, S. Booneveld, J.R. Pels, D.F. Bakker, M.J.F.M. Verhaak, Appl. Catal. B 31 (2001) 73.
[6] P. Ratnasamy, R. Kumar, Catal. Today 9 (1991) 329.
[7] H.Y. Chen, W.M.H. Sachtler, Catal. Today 42 (1998) 73.
[8] G.I. Panov, CATTECH 4 (2000) 18.
[9] J. Pérez-Ramírez, E.V. Kondratenko, Chem. Commun. (2003) 2152.
[10] M. Kogel, R. Monnig, W. Schwieger, A. Tissler, T. Turek, J. Catal. 182 (1999) 470.
[11] J. Jia, K.S. Pillai, W.M.H. Sachtler, J. Catal. 221 (2004) 119.
[12] R.Q. Long, R.T. Yang, J. Catal. 201 (2001) 145.
[13] D. Meloni, R. Monaci, V. Solinas, G. Berlier, S. Bordiga, I. Rossetti, C. Oliva, L. Forni, J. Catal. 214 (2003) 169.
[14] G. Centi, P. Ciambelli, S. Perathoner, P. Russo, Catal. Today 75 (2002) 3.
[15] X. Feng, W.K. Hall, Catal. Lett. 41 (1996) 45.
[16] J. Pérez-Ramírez, F. Kapteijn, G. Mul, J.A. Moulijn, Chem. Commun. (2001) 693.
[17] G.I. Panov, V.I. Sobolev, A.S. Kharitonov, J. Mol. Catal. 61 (1990) 85.
[18] J.C. Groen, A. Brückner, E. Berrier, L. Maldonado, J.A. Moulijn, J. Pérez-Ramírez, J. Catal. 243 (2006) 212.
[19] J.-H. Park, J.-H. Choung, I.-S. Nam, S.-W. Ham, Appl. Catal. B 78 (2008) 342.
[20] G.D. Pirngruber, L. Frunz, J.A.Z. Pieterse, J. Catal. 243 (2006) 340.
[21] J.A.Z. Pieterse, S. Booneveld, R.W. van den Brink, Appl. Catal. B 51 (2004) 215.
[22] A. Ribera, I.W.C.E. Arends, S. de Vries, J. Pérez-Ramírez, R.A. Sheldon, J. Catal. 195 (2000) 287.
[23] J. Pérez-Ramírez, F. Kapteijn, J.C. Groen, A. Doménech, G. Mul, J.A. Moulijn, J. Catal. 214 (2003) 33.
[24] J. Pérez-Ramírez, F. Kapteijn, G. Mul, J.A. Moulijn, Appl. Catal. B 35 (2002) 227.
[25] F. Gramm, Ch. Baerlocher, L.B. McCusker, S.J. Warrender, P.A. Wright, B. Han, S.B. Hong, Z. Liu, T. Ohsuna, O. Terasaki, Nature 44 (2006) 79.
[26] S.B. Hong, H.-K. Min, C.-H. Shin, P.A. Cox, S.J. Warrender, P.A. Wright, J. Am. Chem. Soc. 219 (2007) 10870.
[27] S.B. Hong, E.G. Lear, P.A. Wright, W. Zhou, P.A. Cox, C.-H. Shin, J.-H. Park, I.-S. Nam, J. Am. Chem. Soc. 126 (2004) 5817.
[28] Ch. Baerlocher, F. Gramm, L. Massüger, L.B. McCusker, Z. He, S. Hovmöller, X. Zou, Science 315 (2007) 1113.
[29] S.-H. Lee, D.-K. Lee, C.-H. Shin, Y.-K. Park, P.A. Wright, W.M. Lee, S.B. Hong, J. Catal. 215 (2003) 151.
[30] J. Pérez-Ramírez, G. Mul, F. Kapteijn, J.A. Moulijn, A.R. Overweg, A. Doménech, A. Ribera, I.W.C.E. Arends, J. Catal. 207 (2002) 113.
[31] J. Pérez-Ramírez, J.C. Groen, A. Brückner, M.S. Kumar, U. Bentrup, M.N. Debbagh, L.A. Villaescusa, J. Catal. 232 (2005) 318.
[32] H.-K. Min, M.B. Park, S.B. Hong, J. Catal. 271 (2010) 186.
[33] B. Ravel, M. Newville, J. Synchrotron Radiat. 12 (2005) 537.
[34] M. Newville, P. Livins, Y. Yacoby, J.J. Rehr, E.A. Stern, Phys. Rev. B 47 (1993) 14126.
[35] A.L. Ankudinov, J.J. Rehr, J.J. Low, S.R. Bare, Top. Catal. 18 (2002) 3.
[36] S.J. Cho, S.K. Kang, J. Phys. Chem. B 104 (2000) 8124.
[37] S.J. Cho, J. Lee, Y.S. Lee, D.P. Kim, Catal. Lett. 109 (2006) 181.
[38] S.I. Zabinsky, J.J. Rehr, A. Ankudinov, R.C. Albers, M.J. Eller, Phys. Rev. B 52 (1995) 2995.
[39] J. Pérez-Ramírez, F. Kapteijn, G. Mul, X. Xu, J.A. Moulijn, Catal. Today 76 (2002) 55.
[40] G.D. Pirngruber, M. Luechinger, P.K. Roy, A. Cecchetto, P. Smirniotis, J. Catal. 224 (2004) 429.
[41] J. Pérez-Ramírez, M.S. Kumar, A. Brückner, J. Catal. 223 (2004) 13.
[42] J. Pérez-Ramírez, F. Kapteijn, G. Mul, J.A. Moulijn, J. Catal. 208 (2002) 211.
[43] G. Engelhardt, D. Michel, High-Resolution Solid-State NMR of Silicates and Zeolites, Wile, Chichester, 1987.
[44] M. Müller, G. Harvey, R. Prins, Micropor. Mesopor. Mater. 34 (2000) 135.
[45] K. Sun, H. Zhang, Y. Lian, Y. Li, Z. Feng, P. Ying, C. Li, Chem. Commun. (2004) 2480.
[46] E.J.M. Hensen, Q. Zhu, R.A. van Santen, J. Catal. 220 (2003) 260.
[47] E.J.M. Hensen, Q. Zhu, R.A. van Santen, J. Catal. 233 (2005) 136.
[48] K. Sun, H. Xia, Z. Feng, R.A. van Santen, E.J.M. Hensen, C. Li, J. Catal. 254 (2008) 383.
[49] S. Bordiga, R. Buzzoni, F. Geobaldo, C. Lamberti, E. Giamello, A. Zecchina, G. Leofanti, G. Petrini, G. Tozzolo, G. Vlaic, J. Catal. 158 (1996) 486.
[50] G. Lehmann, Z. Phys. Chem. Neue Folge 72 (1970) 279.
[51] Ch. Baerlocher, L.B. McCusker, Database of Zeolite Structures. <http://www.iza-structure.org/databases/>.
[52] El-M. El-Malki, R.A. van Santen, W.M.H. Sachtler, J. Catal. 196 (2000) 212.
[53] El-M. El-Malki, R.A. van Santen, W.M.H. Sachtler, J. Phys. Chem. B 103 (1999) 4611.